Design, Planning, and Control of an Origami-inspired Foldable Quadrotor

Dangli Yang, Shatadal Mishra, Daniel M. Aukes, and Wenlong Zhang*

Abstract— In this paper, a novel foldable quadrotor (FQR) inspired by an origami mechanism is designed. The FQR can fold its arms during flight to enable aggressive turning maneuvers and operations in cluttered environments. A dynamic model of folding is built for this system with the collected data, and a feedback controller is designed to control the position and orientation of the FQR. Lyapunov stability analysis is conducted to show that the system is stable during arm folding and extension, and motion planning of the FQR is achieved based on a modified minimum-snap trajectory generation method. Simulation results are provided to demonstrate the advantage of this design over the conventional quad-rotor in obstacle avoidance during flight.

I. INTRODUCTION

Quadrotors have been studied for over a decade as a low-cost platform with a wide variety of applications including mapping, agriculture, surveillance, and search and rescue. Traditional quadrotors mount motors and electronics on a rigid structure, and this underactuated structure makes it challenging to achieve fast maneuvers, especially in complex environments with multiple obstacles.

Motivated by the limitation of the conventional quadrotor design, several flexible multirotor designs have been proposed and tested. A ballistically-deployable UAV design was proposed to how a quadrotor can be folded and launched into the sky before expanding to perform normal flight operations [1]. The rotors were mounted on 3D-printed arms which can later rotate and act as normal quad-rotor arms. The streamlined shell enabled the UAV to move faster with lower air drag during the launching session. In-flight morphing for multi-rotor UAVs was achieved in [2] where a pulley mechanism was used to rotate the arms of a quadrotor. It was shown that the quadrotor could fold its arms and fly through small holes with a high speed. A scissor-like foldable structure has been studied for a quadrotor to fly through obstacles [3]. Multi-modal robots were also developed based on foldable mechanisms to allow both flying and walking [4]. In addition to structure morphing, the end effectors on a normal UAV could employ foldable structures to save space or achieve special goals, such as carrying cargo [5] and grasping objects [6]. Another degree of flexibility comes from tilting

[1]D. Yang is with with the School for Engineering of Matter, Transport, and Energy, Ira A. Fulton Schools of Engineering, Arizona State University, Tempe, AZ, 85287, USA. Email: `dangli.yang@asu.edu`.

[2]S. Mishra, D. M. Aukes, and W. Zhang are with The Polytechnic School, Ira A. Fulton Schools of Engineering, Arizona State University, Mesa, AZ, 85212, USA. Email: `smishr13@asu.edu`, `daniel.aukes@asu.edu`, `wenlong.zhang@asu.edu`.

*Address all correspondence to this author. The first two authors have equal contribution to this work.
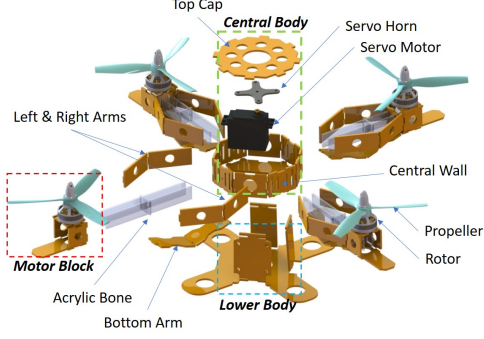
Fig. 1: Origami-inspired FQR prototype.

mechanisms for the motors [7], and they allow the motor thrusts and moments to act on different orientations, enabling very versatile flying patterns. Studies have been conducted on the modeling and motion control of multi-rotors with tilting mechanisms for stability and power efficiency [8].

In this paper, we add one more degree of freedom to a quadrotor with inspirations from the origami mechanism. Origami-inspired, folding, and laminate devices have been demonstrated in a variety of robotic applications, from flapping-wing flying robots at the millimeter scale [9] to terrestrial robots at the millimeter [10] and centimeter scales [11]. These robots utilize a multilayer manufacturing approach to facilitate the creation of flexure-based hinges which can be modeled as revolute joints. These techniques have been used in a walking/flying quad-rotor design which permits a small UAV to alternate between walking and flying while grasping small objects [12]. While many foldable robots utilize laminate, foldable strategies for transmitting power through linkages, most have not looked at how these fabrication techniques can be used to reconfigure the structures of more traditional quadrotors to enhance performance and stability. To the best of the authors' knowledge, this is the first work in literature that utilizes a laminate origami structure for in-flight morphing. The main contributions of this paper are summarized as follows:

- A new foldable quadrotor (FQR) design is proposed based on the laminate origami structure. The FQR structure is made of laser-cut cardboard, which significantly reduces the cost and shortens the fabrication time.
- A dynamic model of the folding mechanism is developed, and a feedback controller is designed with a Lyapunov stability approach to guarantee stability

Fig. 2: Components of the Origami-inspired FQR.

Fig. 3: Geometry and mechanical principle of the servo-arm mechanism.

during in-flight arm folding and extension.

- The minimum-snap trajectory generation technique is extended to plan for the folding actions. Simulation results demonstrate the difference of trajectories when a FQR and conventional quadrotor fly through obstacles.

The remainder of this paper is organized as follows. Section II details the design, fabrication, and aerodynamic analysis of the FQR. In Section III, dynamic models of the folding mechanism and the entire FQR are developed. Section IV discusses the feedback controller design and stability analysis, and Section V presents simulation results. Section VI concludes this paper and discusses future work.

II. DESIGN OF THE FQR

A. Origami and Thread-actuated Mechanism Design

An origami mechanism uses laminate structure to create hinges, springs or other traditional mechanical components [6]. The benefits of this process include saving space, reducing weight, and accelerating the manufacturing process. However, since the connections between different layers are usually through heat adhesive, and the layer materials are usually thin layer of cardboard polymer or fiberglass, the force and moment that the origmai structure (especially the hinges) can undertake before large displacement or structural damage happen are very limited [13]. In the current FQR design, the hinges of each arm function as springs with changing spring constants because their stiffness and duration will be influenced by fatigue.

A prototype of FQR is shown in Fig. 1 with its exploded view shown in Fig. 2. The vehicle is divided into central body, lower body, motor blocks with the acrylic bones, and arms that connect the motor blocks to the central body. A servo motor is placed at the center of the central body with a cross-shape servo horn installed. The acrylic bones connect the motor blocks to the central body to avoid bending of the arms due to gravity of the motor blocks during flight. To allow in-flight folding and extending of the arms, we use a thread-actuated design to pull back the motor block on each arm. Thread actuation is flexible and can be wired and
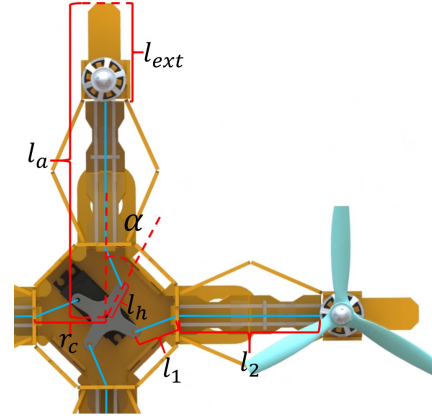
mounted through complex structure [14]. The principle of the thread-actuated design is shown in Fig. 3. The notations and constants used in the figures and calculation are listed in Table I. One end of the thread is mounted on the servo horn and the other end is mounted on the motor block. When the servo motor rotates, the servo horn withdraws the threads and the motor blocks are pulled closer to the center of the FQR. When the servo motor reaches its maximum traveling distance and starts rotating in the opposite direction, because of the origami structure's spring effect, the arms will try to morph back to its original shape and the motor block will be pushed away from the center of the FQR.

B. Manufacturing Process

The FQR frame is made from 6 ply cardboards, mylar and acetate sheet and heat adhesive. All the layers are cut separately using a laser cutter. The four layers of cardboard function as the support structure of the mechanism. The mylar and acetate sheet, which is flexible and durable, functions as hinges and connects all the separate sections together. The heat adhesive is placed between each of the two

TABLE I: Variables and constants of the FQR

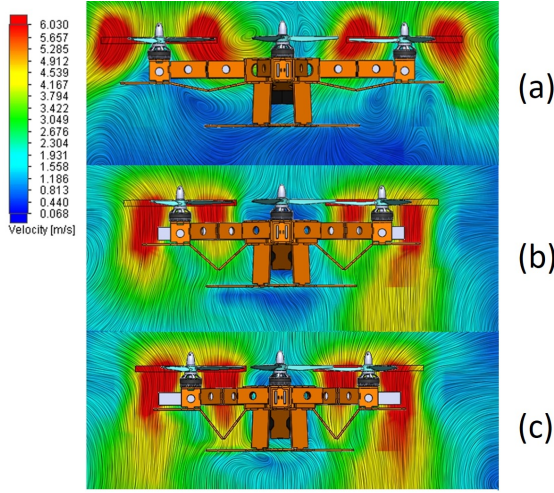| Constants and Variables' Name	Notation
String length	$l_{str} \in \mathbb{R}^+$
Servo horn radius, Central body radius	$l_h, r_c \in \mathbb{R}^+$
Extended arm length, Arm length	$l_{ext}, l_a \in \mathbb{R}^+$
String length from servo horn to central wall	$l_1 \in \mathbb{R}^+$
String length from central wall to motor block	$l_2 \in \mathbb{R}^+$
Servo motor angle, Motor angle to control arm length	$\alpha, u_5 \in \mathbb{R}^+$
Total thrust	$u_1 \in \mathbb{R}^+$
Moment of the three axis in body frame	$u_2, u_3, u_4 \in \mathbb{R}^+$
Rotation matrix of the FQR	$R \in \mathbb{R}^{3 \times 3}$
Angular velocity in the inertial frame	$\omega \in \mathbb{R}^3$
Thrust, Moment from each group of motor and propeller	$F_i, M_i \in \mathbb{R}^+$
Actual / desired moment of inertia matrix	$J / J_d \in \mathbb{R}^{3 \times 3}$
(Maximum) error between $\bar{J}$ and J_d	$J_M / \tilde{J} \in \mathbb{R}^{3 \times 3}$

Fig. 4: Flow simulation results of the FQR surrounding airflow velocity. The foldable arm of the quad-rotor is 0%, 50%, and 100% withdrawn in (a), (b), and (c), respectively.

Fig. 5: Axes and frames of the FQR.

layers to connect them tightly. The FQR's main structure is composed by four pieces of laminate structures: central body and arms, lower body, top cap, and central wall.

C. Aerodynamic Analysis of the FQR

Based on the CAD model, we use SoildWorks Flow Simulation to analyze the surrounding air flow condition of the FQR, where we maintain the FQR steadily at the same location but change the arm length to 0% withdrawn (fully extended), 50% withdrawn and 100% withdrawn (fully folded) during three different simulations. The air flow is only driven by the rotation of the four propellers and the surrounding boundary conditions are set to be steady atmospheric pressure. The results are shown in Fig. 4.

When the FQR's arms are fully extended, the horizontal ambient air flows at much higher velocity compared to the 50% and 100% withdrawn cases. However, the air below the FQR shows lower velocity compared to the other two groups. From the simulation results, when the FQR's arms are fully expanded, the ground effect below the FQR will be less significant and it can provide the FQR with better controllability when operating close to the ground [15]. When the FQR's arms are withdrawn, the ground effect is more significant but the surrounding air flow is slower which results in less turbulence and better controllability in smaller space. When its size is smaller, it can also fly through holes or gaps that are too small for its original size to bypass.

III. MODELING OF THE FQR

A. Coordinates and Notation

To model and control the FQR, we set up a world frame and a body frame [16] as shown in Fig. 5. X_W, Y_W, and Z_W are the three axes in the inertial frame or world frame, which do not change or move during the flight of the FQR. The body frame, which includes X_B, Y_B, and Z_B, will translate and rotate along with the FQR. For each group of the rotor
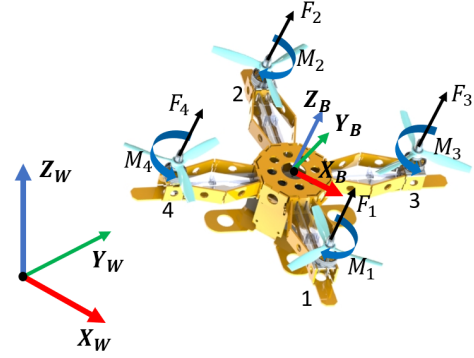
and propeller, the thrust and moment generated are F_i and M_i with respect to the notation number of the rotor.

B. Identification of Arm Length Dynamics

The arm length of the FQR is controlled by a MG996R servo motor. When working under a constant load, the servo motor will maintain a constant rotation speed, and as the load increases, the servo rotation speed will slow until stalling. In this paper, we run some bench tests to perform system identification with a VICON motion capture system. Since a servo motor is used, the input and output of the model are the desired motor angle and actual arm lengths, respectively.

To calculate the desired motor angle, we start with calculating the corresponding servo angle based on the geometry relationship in Fig. 3 and Table I.

$$\begin{cases} l_{str} = l_1 + l_2 \\ l_1 = \sqrt{(l_h sin\alpha)^2 + (r_c - l_h cos\alpha)^2} \end{cases} \quad (1)$$

Since we can measure l_{str}, we can have the expression of arm length l_a as follows:

$$\begin{aligned} l_a &= l_{str} + l_{ext} + r_c - \sqrt{(l_h sin\alpha)^2 + (r_c - l_h cos\alpha)^2} \\ &= l_{str} + l_{ext} + r_c - \sqrt{l_h^2 + r_c^2 - 2r_c cos(\alpha)} \end{aligned} \quad (2)$$

From (2), we are able to calculate the motor angle command given desired arm length. We collect the arm's step response and with the system identification toolbox from MATLAB, we identify the following second-order arm length dynamics. In this paper, the time domain index t is omitted for brevity.

$$\ddot{l}_a = -13.88\dot{l}_a - 77.40l_a + 73.84u_5, \quad (3)$$

and this system has a bandwidth of 1.18 Hz, which presents a limit on how fast the arm can be folded or extended given the chosen servo motor as well as the material and design.

C. Complete Dynamics of the FQR

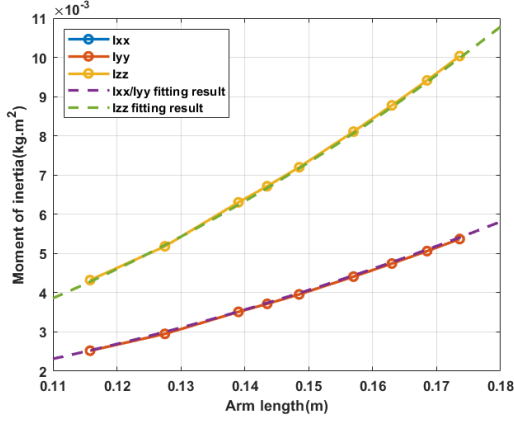Adding the servo-arm dynamics into the original quad-rotor system dynamics [16], the complete FQR system

Fig. 6: Fitting of moment of inertia with arm length changes.

dynamics can be described as $\dot{\mathbf{x}} = \mathbf{f}(\mathbf{x}) + \mathbf{g}(\mathbf{x})\mathbf{u}$:

$$
\begin{bmatrix} \ddot{r} \\ \dot{r} \\ \dot{\omega} \\ \dot{\theta} \\ \ddot{l}_a \\ \dot{l}_a \end{bmatrix} = \begin{bmatrix} -g\mathbf{Z_W} + \frac{u_1}{m}\mathbf{Z_B} \\ \dot{r} \\ J(l_a)^{-1} \left[-\omega_{BW} \times J(l_a)\omega_{BW} + \begin{bmatrix} u_2 \\ u_3 \\ u_4 \end{bmatrix} \right] \\ \omega \\ -13.88\dot{l}_a - 77.40 l_a + 73.84 u_5 \\ \dot{l}_a \end{bmatrix} \quad (4)
$$

where $\mathbf{x} = \begin{bmatrix} \dot{r} & r & \omega & \theta & \dot{l}_a & l_a \end{bmatrix}^T \in \mathbb{R}^{14}$ and $\mathbf{u} \in \mathbb{R}^5$. Since the moment of inertia change with the arm length, the J matrix is now functions of arm length l_a. To find out the relation between the arm length and moment of inertia, a traditional way is to calculate every component's moment of inertia and sum them up to obtain the total moment of inertia. However, origami structure has very complex geometry and to simplify the calculation many assumptions need to be made. To improve the estimation accuracy, we use SolidWorks Mass-Property toolbox to obtain $J(l_a)$ when the FQR's arms are withdrawn at different percentages. Based on the experimental data, we are able to do parabolic fitting and obtain the relation between arm length and moment of inertia as shown in (5). Experimental data and fitting results are shown in Fig. 6.

$$
\begin{cases} J_{xx} = J_{yy} = 0.205 l_a^2 - 0.0095 l_a + 0.00088, \\ J_{zz} = 0.41 l_a^2 - 0.02 l_a + 0.0011, \end{cases} \quad (5)
$$

where $0.0025 \leqslant J_{xx} = J_{yy} \leqslant 0.0054$ and $0.0043 \leqslant J_{zz} \leqslant 0.0100$ because the arm length can only be changed within a certain range. After defining the dynamic system of the FQR, to calculate the rotating speed of each motor, we use the following equation set from [16], in which k_F and k_M are rotor thrust and rotor moment constants respectively.

$$
\begin{bmatrix} u_1 \\ u_2 \\ u_3 \\ u_4 \end{bmatrix} = \begin{bmatrix} 1 & 1 & 1 & 1 \\ 0 & k_F l_a & 0 & -k_F l_a \\ -k_F l_a & 0 & k_F l_a & 0 \\ k_M & -k_M & k_M & -k_M \end{bmatrix} \begin{bmatrix} \omega_1^2 \\ \omega_2^2 \\ \omega_3^2 \\ \omega_4^2 \end{bmatrix} \quad (6)
$$

$$
F_i = k_F \omega_i^2, \ M_i = k_M \omega_i^2 \quad (7)
$$

It should be noted that l_a now is one of the state in the dynamics system and it is controlled by u_5 in (3).

IV. CONTROLLER DESIGN AND STABILITY ANALYSIS

This section introduces feedback controller design and Lyapunov stability analysis for the FQR model defined in (4). With this controller, the FQR will be able to follow the planned trajectory with arm folding/extension, and the closed-loop system will be robust to the modeling uncertainties caused by the changes of arm length. We first introduce the following translational position and velocity errors, as well as orientation and body frame rotational velocity errors:

$$
e_x = x - x_d, \quad (8)
$$
$$
e_v = v - v_d, \quad (9)
$$
$$
e_R = \frac{1}{2}(R_d^T R - R^T R_d)^\vee, \quad (10)
$$
$$
e_\Omega = \Omega - R^T R_d \Omega_d. \quad (11)
$$

Note that in (10) the vee map "$\vee$" is the inverse operator of hat operator, which transforms a matrix back to a vector.

Inspired by [17], we use the Lyapunov stability method to prove that the FQR is stable and the error for both translational and rotational movement can converge. Because of the additional one degree of freedom of the FQR, the rotational dynamics of the FQR is different from a normal quad-rotor. Since the FQR has the same position control loop dynamics, the force input and stability proof in the position loop are the same as [17]. However, we have to modify the moment input to account for the changing arm length in the attitude control loop. We start by defining the control inputs to the system. The notations can be found in Table I.

$$
F = -(-k_x e_x - k_v e_v - mge_3 + m\ddot{x}_d) \cdot Re_3, \quad (12)
$$
$$
M_a = -k_R e_R - k_\Omega e_\Omega - J_d(\hat{\Omega} R^T R_d \Omega_d - R^T R_d \dot{\Omega}_d) \quad (13)
$$
$$
+ \Omega \times J_d \Omega - ||e_A|| J_M(||\alpha_d|| + ||\Omega||^2||),
$$

where $e_A = e_\Omega + c e_R$, $\alpha_d = \hat{\Omega} R^T R_d \Omega_d - R^T R_d \dot{\Omega}_d$. Moreover, c satisfies

$$
c < \min \left\{ \sqrt{\frac{2b_1 k_R \lambda_m}{\lambda_M^2}}, \frac{\sqrt{2}(k_\Omega - \frac{1}{2}J_B)}{3\lambda_M}, \frac{k_R k_\Omega - \frac{1}{2}J_B k_R}{\frac{1}{4}(k_\Omega - J_B)^2 + \frac{3k_B}{\sqrt{2}}\lambda_M} \right\}
$$

Proof: Due to the page limit, we will only show a sketch of the proof, which is inspired by [18]. In this paper, the following Lyapunov function candidate is used:

$$
V = \frac{1}{2}e_\Omega^T J e_\Omega + k_R \Psi(R, R_d) + c e_\Omega^T J e_R, \quad (14)
$$

where c is a constant. Let $\zeta = [||e_R||, ||e_\Omega||]^T \in \mathbb{R}^2$, and based on [18] one can get $V \geqslant \zeta^T P \zeta$ with

$$
P = \begin{bmatrix} b_1 k_R & \frac{1}{2}c\lambda_M \\ \frac{1}{2}c\lambda_M & \frac{1}{2}\lambda_m \end{bmatrix},
$$

and it was shown in [18] that $\Psi(R, R_d) \geqslant b_1 ||e_R(R, R_d)||^2$. λ_M and λ_m are the largest and smallest eigenvalues of J,

respectively. The next step is to prove $\dot{V}$ is negative definite.

$$\dot{V} = e_\Omega^T J \dot{e}_\Omega + \frac{1}{2} e_\Omega^T \dot{J} e_\Omega + k_R e_R^T e_\Omega + c e_\Omega^T J \dot{e}_R \qquad (15)$$
$$+ c e_R^T J \dot{e}_\Omega + c e_\Omega^T \dot{J} e_R$$

Since the moment of inertia, J, is no longer a constant, the derivative matrix of J can be calculated as follows:

$$\dot{J}(l_a) = \left[J'_{ij} \dot{l}_a \right]_{i,j=1,2,3} \qquad (16)$$

As seen in (2), the relation between the servo motor angle and arm length is linked geometrically, the derivation of the arm length can be calculated as below:

$$-\frac{\pi}{42} \leqslant \dot{l}_a = -\frac{\dot{\alpha} a_1 \sin\alpha}{2\sqrt{a_2 - a_1 \cos\alpha}} \leqslant \frac{\pi}{42}, \qquad (17)$$

where $a_1 = 2 r_c l_h$, $a_2 = l_h^2 + r_c^2$. Therefore, $\dot{J}$ is bounded and the 2-norm of the bound matrix is J_B.

Based on the dynamic model (4) and error definition (11), it can be derived that

$$J\dot{\Omega} = (M_a - \Omega \times J\Omega) \qquad (18)$$
$$J\dot{e}_\Omega = J\dot{\Omega} + J(\hat{\Omega} R^T R_d \Omega_d - R^T R_d \dot{\Omega}_d) \qquad (19)$$
$$= M_a - \Omega \times J\Omega + J\left(\hat{\Omega} R^T R_d \Omega_d - R^T R_d \dot{\Omega}_d\right)$$

Now substituting the control input of M_a defined in (13) into the equation above, one can reach:

$$J\dot{e}_\Omega = -k_R e_R - k_\Omega e_\Omega + \Omega \times \tilde{J}\Omega + \tilde{J}\alpha_d \qquad (20)$$
$$-\|e_A\| J_M (\|\alpha_d\| + \|\Omega\|^2\|),$$

where $\tilde{J} = J - J_d$. Since both J_d and J are bounded, $\tilde{J}$ is also bounded and the 2-norm of upper bound matrix is defined as J_M, Now plug (20) into (15), the derivative of V is derived as follows:

$$\dot{V} = -k_\Omega \|e_\Omega\|^2 - c k_R \|e_R\|^2 \qquad (21)$$
$$+ e_A^T (\tilde{J}\alpha_d + \Omega \times \tilde{J}\Omega)$$
$$+ c e_\Omega^T J \dot{e}_R + e_R^T (c\dot{J} - c k_\Omega I_3) e_\Omega + \frac{1}{2} e_\Omega^T \dot{J} e_\Omega$$
$$- \|e_A\| J_M (\|\alpha_d + \|\Omega\|^2\|),$$

Based on the definition of sgn function and Cauchy-Schwarz inequality, one can find the following bounds for the items in the above equation:

$$e_A^T \tilde{J}\alpha_d \leqslant J_M \|e_A\| \cdot \|\alpha_d\|,$$
$$e_A^T \left(\Omega \times \tilde{J}\Omega\right) \leqslant J_M \|e_A\| \cdot \|\Omega\|^2.$$

Therefore, the third and seventh items of (21) get canceled out, and we get

$$\dot{V} \leqslant -k_\Omega \|e_\Omega\|^2 - c k_R \|e_R\|^2 \qquad (22)$$
$$+ c e_\Omega^T J \dot{e}_R + e_R^T (c\dot{J} - c k_\Omega I_3) e_\Omega + \frac{1}{2} e_\Omega^T \dot{J} e_\Omega$$

Considering the bound of $\dot{J}$, the inequality above can be further constrained as

$$\dot{V} \leqslant -k_\Omega \|e_\Omega\|^2 - c k_R \|e_R\|^2 \qquad (23)$$
$$+ c e_\Omega^T J \dot{e}_R + c (J_B - k_\Omega) \|e_R\| \cdot \|e_\Omega\| + \frac{1}{2} J_B \|e_\Omega\|^2$$
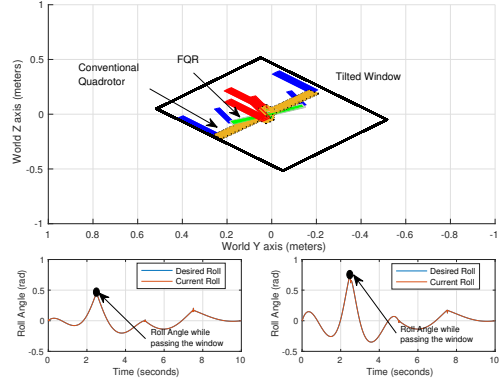

Fig. 7: Orientation of the FQR and conventional quad-rotor when flying through the window (top); Planned and actual roll angles of the FQR during the flight (bottom left); Planned and actual roll angles of the conventional quad-rotor during flight (bottom right).

The rest of the proof follows [18] and details are omitted, and one can get $\dot{V} \leqslant -\zeta^T Q \zeta$, where

$$Q = \begin{bmatrix} c k_R & \frac{c(k_\Omega - J_B)}{2} \\ \frac{c(k_\Omega - J_B)}{2} & k_\Omega - \frac{3c}{\sqrt{2}} \lambda_M - \frac{1}{2} J_B \end{bmatrix}$$

Therefore, to make $P > 0$ and $Q < 0$, the constraints for c is identified. This completes the proof.

V. SIMULATION RESULTS

This section demonstrates the performance of trajectory planning and feedback control using simulation results. It demonstrates how the FQR design can affect the planned trajectory with arm bending while flying through obstacles.

In this work, we employ the minimum snap trajectory planning method to generate trajectory for the FQR [16]. However, unlike conventional quad-rotors, l_a and its derivatives are also states of the state space model of the FQR as can be noticed in (4), u_5 is the input to the horn motor that controls the arm length of the FQR. Therefore it is obvious that in addition to x, y, z and ψ (yaw angle), l_a is also one flat output of the system. Let $\Phi = [x, y, z, \psi, l_a]^T$, the objective function for motion planning is modified as follows:

$$\min_\Phi \int_{t_0}^{t_m} \mu_r \|\frac{d^{k_r} r_T}{dt^{k_r}}\|^2 + \mu_\psi (\frac{d^{k_\psi} \psi_T}{dt^{k_\psi}})^2 + \mu_{l_a} (\frac{d^{k_{l_a}} l_a}{dt^{k_{l_a}}})^2, \qquad (24)$$
$$x(1) = (0,0,0), \quad \dot{x}(1) = (0,0,0), \quad \ddot{x}(1) = (0,0,0)$$
$$x(2) = (2,0,0), \quad \dot{x}(2) = (0.1,0,0), \quad \ddot{x}(2) = (0,9.8,0)$$
$$x(3) = (2,3,0), \quad \dot{x}(3) = (1.0,0,0), \quad \ddot{x}(3) = (0,0,0)$$
$$x(4) = (0,0,0), \quad \dot{x}(4) = (0,0,0), \quad \ddot{x}(4) = (0,0,0)$$

where t_0 and t_m are the start and end time for motion planning, μ_r, μ_ψ and μ_{l_a} are the weighting factors. As for the constraints, the number inside the brackets indicate the corresponding waypoint number, so in this case we have four waypoints. In [16], the author selected k_r to be 4 because of the target of minimizing the square of the norm of the snap.

For k_ψ, since the input u_4 appear in the second derivative, k_ψ is chosen to be 2. In the FQR case, as shown in (3), u_5 also appear in the second derivative, so k_{l_a} is also selected to be 2. Here we present some simulation results. In the simulation, the FQR will remain on the same height (z is the same throughout the entire trajectory) and travel along the x axis to fly through a tilted window. The window width is large enough for the FQR to pass without collision, but the height will be comparatively limited. The FQR uses (24) to generate trajectory and low-level motion controller (12) and (13) is implemented. For comparison, a conventional quadrotor case was shown, where motion planning was conducted using the same method without considering arm folding, and motion control follows [17].

As shown in Fig. 7, when the FQR flies through the window, it folds its arms and the rolling angle is much smaller than that of the conventional quadrotor, which reduces the energy cost and risk of hitting the window frame due to imperfect motion control. It is also demonstrated that the low-level feedback controller could track the desired roll angle perfectly. Fig. 8 shows the entire trajectory with three waypoints based on the minimum snap trajectory generation shown in (24). With the foldable arms, the FQR can achieve smaller roll angles for obstacle avoidance, and shorter yet smoother trajectory, compared to a conventional quadrotor.
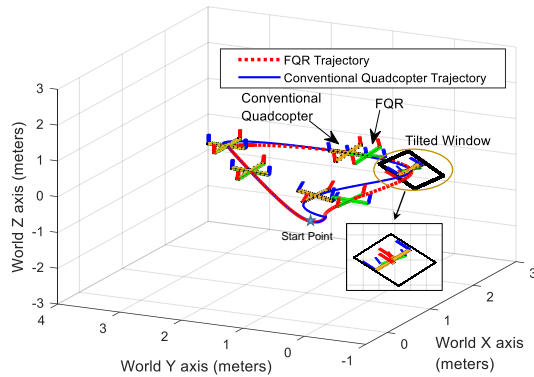

Fig. 8: Trajectory planning of FQR and conventional quadrotor to fly through a tilted window.

VI. Conclusion and future work

In this paper, an origami-inspired FQR was developed using cardboard. With its arms extended or folded, the FQR could change the moment of inertia and ambient air flow velocity. A feedback controller was developed to guarantee stability with changing arm lengths, and the minimum snap trajectory generation approach was extended to plan the position, yaw angle, and the arm length. Simulation results were provided to demonstrate the advantage of this FQR design when flying through obstacles, as well as the precision of position and orientation control of the FQR.

As for future work, multiple airflow simulations will be performed to analyze different dynamic effects caused due to the quadrotor folding. Subsequently, extensive experimental studies will be conducted in both indoor and outdoor environments to evaluate the performance of the FQR. Different materials will be tested in the FQR fabrication to improve the durability and reduce possible vibration from the motors. The origami structure will also be used to achieve in-flight morphing, such as arm tilting and rotation.

References

[1] L. Henderson, T. Glaser, and F. Kuester, "Towards bio-inspired structural design of a 3d printable, ballistically deployable, multi-rotor uav," in *Aerospace Conference, 2017 IEEE*. IEEE, 2017, pp. 1–7.

[2] V. Riviere, A. Manecy, and S. Viollet, "Agile robotic fliers: A morphing-based approach," *soft robotics*, 2018.

[3] N. Zhao, Y. Luo, H. Deng, and Y. Shen, "The deformable quadrotor: Design, kinematics and dynamics characterization, and flight performance validation," in *Intelligent Robots and Systems, 2017 IEEE/RSJ International Conference on*. IEEE, 2017, pp. 2391–2396.

[4] S. Mintchev and D. Floreano, "A multi-modal hovering and terrestrial robot with adaptive morphology," in *Proceedings of the 2nd International Symposium on Aerial Robotics*, no. CONF, 2018.

[5] P. M. Kornatowski, S. Mintchev, and D. Floreano, "An origami-inspired cargo drone," in *IEEE/RSJ International Conference on Intelligent Robots and Systems*, no. EPFL-CONF-230988, 2017.

[6] S.-J. Kim, D.-Y. Lee, G.-P. Jung, and K.-J. Cho, "An origami-inspired, self-locking robotic arm that can be folded flat," *Science Robotics*, vol. 3, no. 16, p. eaar2915, 2018.

[7] C. Hintz, C. Torno, and L. R. G. Carrillo, "Design and dynamic modeling of a rotary wing aircraft with morphing capabilities," in *Unmanned Aircraft Systems, 2014 International Conference on*. IEEE, 2014, pp. 492–498.

[8] C. Holda, B. Ghalamchi, and M. W. Mueller, "Tilting multicopter rotors for increased power efficiency and yaw authority," in *2018 International Conference on Unmanned Aircraft Systems*. IEEE, 2018, pp. 143–148.

[9] K. Y. Ma, P. Chirarattananon, S. B. Fuller, and R. J. Wood, "Controlled Flight of a Biologically Inspired, Insect-Scale Robot," *Science*, vol. 340, no. 6132, pp. 603–607, may 2013.

[10] B. Goldberg, N. Doshi, K. Jayaram, and R. Wood, "Gait studies for a quadrupedal microrobot reveal contrasting running templates in two frequency regimes," *Bioinspiration & Biomimetics*, vol. 12, no. 1, 2017.

[11] D. W. Haldane, K. C. Peterson, F. L. Garcia Bermudez, and R. S. Fearing, "Animal-inspired design and aerodynamic stabilization of a hexapedal millirobot," *2013 IEEE International Conference on Robotics and Automation*, pp. 3279–3286, 2013.

[12] J.-s. Koh, D. M. Aukes, B. Araki, S. Pohorecky, Y. Mulgaonkar, M. T. Tolley, V. Kumar, D. Rus, and R. J. Wood, "A Modular Folded Laminate Robot Capable of Multi Modal Locomotion," *ISER 2016*, vol. 1, pp. 1–12, 2017.

[13] I. L. Delimont, S. P. Magleby, and L. L. Howell, "Evaluating compliant hinge geometries for origami-inspired mechanisms," *Journal of Mechanisms and Robotics*, vol. 7, no. 1, p. 011009, 2015.

[14] E. Vander Hoff, D. Jeong, and K. Lee, "Origamibot-i: A thread-actuated origami robot for manipulation and locomotion," in *Intelligent Robots and Systems, 2014 IEEE/RSJ International Conference on*. IEEE, 2014, pp. 1421–1426.

[15] P. E. Pounds, D. R. Bersak, and A. M. Dollar, "Stability of small-scale uav helicopters and quadrotors with added payload mass under pid control," *Autonomous Robots*, vol. 33, no. 1-2, pp. 129–142, 2012.

[16] D. Mellinger and V. Kumar, "Minimum snap trajectory generation and control for quadrotors," in *Robotics and Automation, 2011 IEEE International Conference on*. IEEE, 2011, pp. 2520–2525.

[17] T. Lee, M. Leoky, and N. H. McClamroch, "Geometric tracking control of a quadrotor uav on se (3)," in *Decision and Control, 2010 49th IEEE Conference on*. IEEE, 2010, pp. 5420–5425.

[18] T. Fernando, J. Chandiramani, T. Lee, and H. Gutierrez, "Robust adaptive geometric tracking controls on so (3) with an application to the attitude dynamics of a quadrotor uav," in *Decision and Control and European Control Conference, 2011 50th IEEE Conference on*. IEEE, 2011, pp. 7380–7385.